Shortwave TOA Cloud Radiative Forcing Derived from a Long-Term (1980–Present) Record of Satellite UV Reflectivity and CERES Measurements

CLARK WEAVER

Earth System Science Interdisciplinary Center, University of Maryland, College Park, College Park, and Atmospheric Chemistry and Dynamics Branch, NASA Goddard Space Flight Center, Greenbelt, Maryland

JAY HERMAN

Joint Center for Earth Systems Technology Center, University of Maryland, Baltimore County, Catonsville, and Atmospheric Chemistry and Dynamics Branch, NASA Goddard Space Flight Center, Greenbelt, Maryland

GORDON LABOW, DAVID LARKO, AND L.-K. HUANG

Science Systems and Applications, Inc., Lanham, and Atmospheric Chemistry and Dynamics Branch, NASA Goddard Space Flight Center, Greenbelt, Maryland

(Manuscript received 7 August 2014, in final form 3 September 2015)

ABSTRACT

A 34-yr record of shortwave top-of-atmosphere (TOA) radiative cloud forcing is derived from UV Lambertian equivalent reflectivity (LER) data constructed using measured upwelling radiances from the *Nimbus-7* Solar Backscatter Ultraviolet (SBUV) and from seven NOAA SBUV/2 instruments on polar-orbiting satellites. The approach is to scale the dimensionless UV LER data to match the CERES shortwave cloud radiative forcing when they are concurrent (2000–13). The underlying trends of this new longer-term CERES-like data record are solely based on the UV LER record. The good agreement between trends and anomalies of the CERES-like and CERES shortwave cloud forcing records during the overlapping data period supports using this new dataset for extended climate studies. The estimated linear trend for the shortwave TOA radiative forcing due to clouds from 60°S to 60°N is $+1.47\ \mathrm{W\,m^{-2}}$ with a 0.11 uncertainty at the 95% confidence level over the 34-yr period 1980–2013.

1. Introduction

Cloud radiative feedback quantifies an aspect of how clouds respond to a warming climate, specifically, the change in the top-of-atmosphere (TOA) reflected radiative flux from changes in cloud amount or morphology (R_{cloud}) per degree temperature change at the earth's surface. Here R_{cloud} is called the cloud radiative forcing (watts per meter squared). Currently, the longest observational data record for shortwave (SW) R_{cloud} is from the International Satellite Cloud Climatology Project (ISCCP; 1983–2009). This project collected radiances from the Advanced Very High Resolution Radiometer (AVHRR) and geostationary weather satellite radiance measurements and analyzed them to infer the global distribution of clouds and their properties. Since the geostationary instruments were designed to gather weather rather than climate information, the spectral response of the many SW sensors that contributed to the record does not cover the entire solar spectrum, and they do not have onboard SW calibration systems. TOA longwave and SW radiative fluxes have been calculated using cloud information along with other observations to generate the ISCCP global radiative flux data (FD) product and are used here to validate our UV Lambertian equivalent reflectivity (LER)–based R_{cloud} product.

Corresponding author address: Clark Weaver, Atmospheric Chemistry and Dynamics Branch, Code 614, NASA Goddard Space Flight Center, Greenbelt, MD 20771.
E-mail: clark.j.weaver@nasa.gov

DOI: 10.1175/JCLI-D-14-00551.1

A calibrated observational record is from the Clouds and the Earth's Radiant Energy System (CERES; 2000 to present). The SW sensor (0.3–5 μm) spans the solar spectrum, and both the shortwave and longwave channels have onboard calibration sources to track the stability of the instruments. Hence, this dataset is more suitable than ISCCP products for studying cloud–climate feedbacks. However, the 14-yr span of the CERES data record limits the study of cloud response to relatively short-term changes in the surface temperature (T_s), which are partly driven by El Niño–Southern Oscillation (ENSO) cycle. We present a 34-yr record of SW TOA cloud radiative forcing derived from the LER using observed upwelling 340-nm radiances. The 340 $\pm$ 1 nm wavelength channel was chosen because it is not significantly sensitive to ozone absorption. For surfaces free of snow and ice, the UV LER is most sensitive to changes in cloud amount, since the UV reflectivity of the earth's surface is small [LER $<$ 0.06 reflectivity units (RU); Herman and Celarier 1997]. This paper discusses the conversion of the dimensionless 340-nm LER data (Herman et al. 2013) into a CERES-like SW cloud radiative forcing product. Although we only provide the shortwave component, the relatively long record means that we can potentially investigate the cloud radiative forcing response from the gradual temperature changes due to greenhouse gases and any other causes, rather than the cloud response from short-term ENSO fluctuations.

2. 34-yr UV reflectivity data record

The Solar Backscatter Ultraviolet (SBUV) observing system is a series of NASA and NOAA polar-orbiting satellite instruments designed to monitor total column and vertical profiles of ozone and to monitor the 340-nm LER. We demonstrate that the channel insensitive to ozone at 340 nm can also provide long-term information on cloud radiative forcing albedo. Our dataset starts in 1980 with *Nimbus-7* SBUV and continues through 2013 using data from seven SBUV/2 instruments.

The primary products of the SBUV instruments are the nadir-viewed narrowband backscatter radiances (I) and the measured solar irradiance (F). Regular sun-viewing irradiance measurements are taken (typically weekly) to provide long-term calibration information.

The top boxed portion of Fig. 1 charts the calculation of UV LER from the SBUV/2 measurements of I and F. Although not part of this study, the calculation of UV LER is briefly presented here to give the reader a sense of past efforts to correct known instrument problems, to intercalibrate the individual instrument records, and to retrieve ozone profile and total column information (green boxes). For additional details on the calibration procedures, see DeLand et al. (2012). The version 8.6 ozone retrieval algorithm is fully described in Bhartia et al. (2013).

a. Calibration and correction

SBUV measurements were corrected for electronic offsets, thermal temperature dependence, nonlinearity, and photomultiplier gain change and then converted to physical units (I, F) with prelaunch photometric calibration. The solar irradiance is measured by deploying a diffuser plate to reflect sunlight into the entrance slit of the monochromator as the satellite crosses the day–night terminator. The solar diffuser is the only element not common to the optical path in the two measurements (I, F). As a result, many factors affecting the instrument sensitivity as well as solar activity variability cancel out in the directional albedo, the ratio of I/F.

1) Diffuser plate darkening

Unfortunately, the solar diffuser is subject to darkening. Since the diffuser reflectivity is still included in I/F, its darkening rate needs to be monitored if long-term trends in ozone and cloud radiative forcing albedo are sought. Uncertainty in the rate of diffuser plate darkening dominates the time-dependent (T.D.) errors—errors that are expected to vary over the life of the instrument. These are shown in Table 1.

The early SBUV technology of *Nimbus-7* did not have an onboard calibration system to track the diffuser reflectivity. Initially, an accelerated exposure time approach was implemented to tease out the darkening rate, but the retrieved ozone total column amounts were inconsistent with ground-based observations. An alternate method was developed that uses the measured I/F from several wavelength pairs to construct an internally self-consistent calibration. The method uses the wavelength dependence of the sensitivity to calibration errors and the requirement that albedo ratios for each wavelength pair yield the same total ozone amounts. This method is termed ''pair justification'' (Herman et al. 1991).

To better monitor the darkening, later SBUV/2 instruments featured an onboard calibration system to track relative changes in diffuser reflectivity using a mercury lamp (Weiss et al. 1991). But problems with the lamp stability motivated an alternative approach that uses the Antarctic Plateau as a stable terrestrial albedo reference (Huang et al. 2003; Jaross and Warner 2008). The Antarctic Plateau offers high surface reflectivity from snow- and ice-covered surfaces, minimal contamination due to clouds and aerosols, and low terrain height variations to minimize the surface bidirectional reflectance

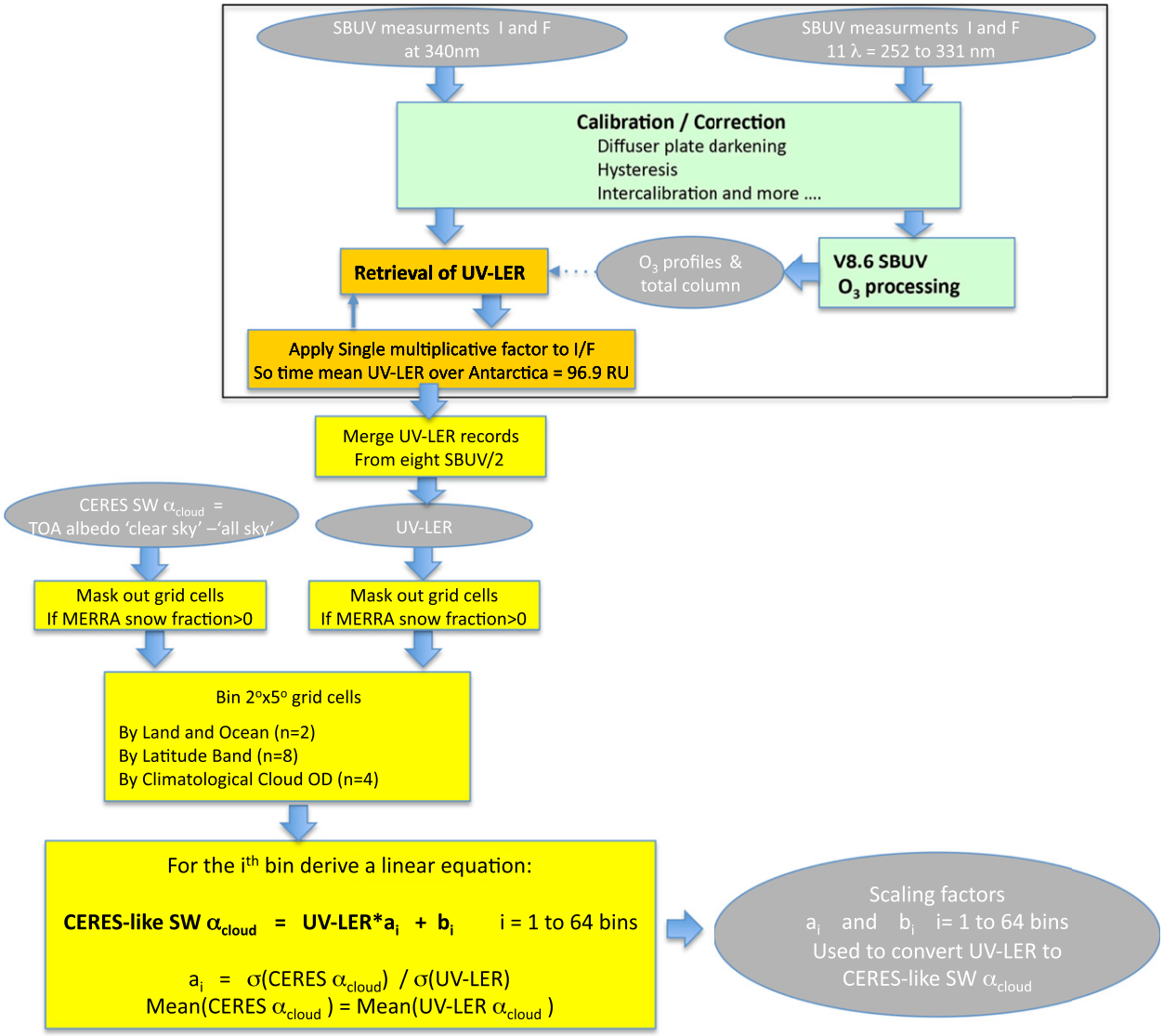

FIG. 1. Flow chart showing derivation of scaling factors (a, b) used to convert UV LER to CERES-like SW α_{cloud}. Input quantities are SBUV measurements of nadir-viewed backscatter radiances (I) and the measured solar irradiance (F). The α_{cloud} is the TOA cloud radiative forcing albedo. Gray ovals are datasets, green boxes are processes dealing with instrument calibration–correction and ozone processing, dark yellow boxes involve generation of UV LER, and yellow boxes are flow chart processes for this study. The four latitude bins for each hemisphere are 60°–45°, 45°–30°, 30°–15°, and 15°–0°. The four cloud optical depth bins are 0–3, 3–4.5, 4.5–6, and >6.

distribution function (BRDF) effects. For some SBUV/2 instruments (*NOAA-14* and *NOAA-16*) there was little difference between the mercury lamp and the Antarctic Plateau approach, but other instruments had up to 3% differences. Here the Antarctic Plateau–derived darkening rate was used in the correction. The mercury lamp on board *NOAA-9* SBUV suffered from poor stability. This rendered the onboard calibration useless, and time-dependent errors for this instrument are 3 times higher than those from other instruments. Table 1 shows which method is used to determine the darkening rate for each SBUV instrument.

2) HYSTERESIS

The *Nimbus-7*, and to a lesser extent the *NOAA-9*, instrument photomultiplier tube (PMT) was not able to respond to the rapid increase in radiance signal when the satellite first emerges from Southern Hemisphere (SH) polar night darkness on each orbit. Uncorrected radiances can be off by 8%–9% at high SH latitudes and their impact can reach to the equator during SH winter. A correction was developed for *Nimbus-7* SBUV by comparing PMT signals with concurrent data from an onboard reference photodiode at 343 nm that

TABLE 1. Instrument: SBUV and SBUV/2 instruments used in our merged UV LER data record. Intercalibration method is the method used to intercalibrate SBUV/2 records (see section 2a). Diffuser plate reflectivity is the method used to determine diffuser plate reflectivity. The possible approaches are pair justification (Herman et al. 1991), mercury (Hg) lamp calibration (Weiss et al. 1991), and calibration using Antarctic snow–ice (Huang et al. 2003). The T.D. error is the time-dependent errors for each SBUV/2 instrument in terms of percent directional albedo I/F. These 1σ errors are taken from DeLand et al. (2012).

Instrument	Intercalibration method	Diffuser plate reflectivity	T.D. error (%)
Nimbus-7	Coincidence with *NOAA-11*, different local time	Pair Justification	1.14
NOAA-9	Coincidence with *NOAA-11*, different local time	Hg lamp (poor stability)	3.63
NOAA-11	Absolute calibration SSBUV-2 (1990) SSBUV-6 (1994)	Antarctic snow/ice	1.19
NOAA-14	SSBUV and coincidence with *NOAA-16*, same local time (better approach)	Hg lamp	1.13
NOAA-16	Coincidence with *NOAA-17*, same local time (better approach)	Hg lamp	0.83
NOAA-17	Absolute calibration prelaunch	Antarctic snow/ice	0.77
NOAA-18	Coincidence with *NOAA-17*, same local time (better approach)	Antarctic snow/ice	0.81
NOAA-19	Coincidence with *NOAA-17*, same local time (better approach)	Hg lamp	0.81

does not have this problem, and the estimated uncertainty after correction is less than 1% (DeLand et al. 2001).

3) INTERCALIBRATION

It is necessary to intercalibrate all the SBUV instruments to generate an accurate long-term ozone record. Both *NOAA-11* and *NOAA-17* instruments are considered benchmarks. *NOAA-11* is calibrated against an SBUV on board the Space Shuttle (SSBUV) in 1990 and 1994 (Hilsenrath et al. 1995). *NOAA-17* prelaunch calibration is tied to laboratory standards. All other instruments are adjusted to minimize differences in coincidence measurements when they temporally overlap. For earlier instruments (*Nimbus-7* and *NOAA-9*) coincident intercalibration with *NOAA-11* was performed at different local times of the day so diurnal cloud changes degrade results. For later instruments, intercalibration with *NOAA-17* can be done at the same local time; this approach is superior.

b. Retrieval of UV LER

The UV LER is retrieved from the intercalibrated and corrected directional albedo at 340 nm, $A = I/F$. Similarly, directional albedos of the shorter SBUV wavelengths are input to the version 8.6 ozone processing algorithm. The UV LER does not include any Rayleigh scattering and the negligible ozone absorption at 340 nm has been removed based on the retrieved ozone amounts. Specifically, the UV LER assumes Lambertian reflection for the entire nadir scene, composed of clouds, aerosols, and the earth's surface, but without the Rayleigh scattering.

Even with the careful intercalibration procedures, a comparison of the overlapping summertime 340-nm LER time series from different SBUV/2 instruments over the Antarctic Plateau show that there were still small differences (typically less than ±0.5%). To correct this, the directional albedos (I/F) of each individual SBUV/2 instrument record were multiplied by a single factor so that the individual record mean over the Antarctic Plateau is 96.9 RU (Herman et al. 2013; see orange boxes in Fig. 1). We are implicitly assuming that there has been no long-term change in the snow–ice reflectivity over the 34-yr period.

We also correct for the estimated diurnal cycle in cloudiness. This might introduce additional trends in the LER, since the eight UV sensing instruments have different equator-crossing times. To correct for this, each individual measurement has been "noontime corrected" based on the local time of the measurement, the instrument's equator-crossing time, and a UV diurnal LER climatology (Labow et al. 2011). Even with this correction we have less confidence in measurements taken early in the morning or late in the day when solar zenith angles are above 80°.

Figure 2 (top) shows the UV LER values in terms of RU (which ranges from 0 to 100) for each individual SBUV/2 instrument used in this study.

c. Merging the SBUV/2 records

Merging of individual SBUV/2 instruments into a cross-calibrated record of UV LER builds off the experience of the ozone team at the Atmospheric Chemistry and Dynamics Branch at NASA Goddard Space Flight Center. They have studied the above-mentioned calibration problems extensively and constructed a merged ozone dataset (MOD) from the SBUV instrument series (http://acdb-ext.gsfc.nasa.gov/Data_services/merged/index.html).

To track the quality of each version of MOD, they rely on the residuals from the version 8.6 ozone retrievals.

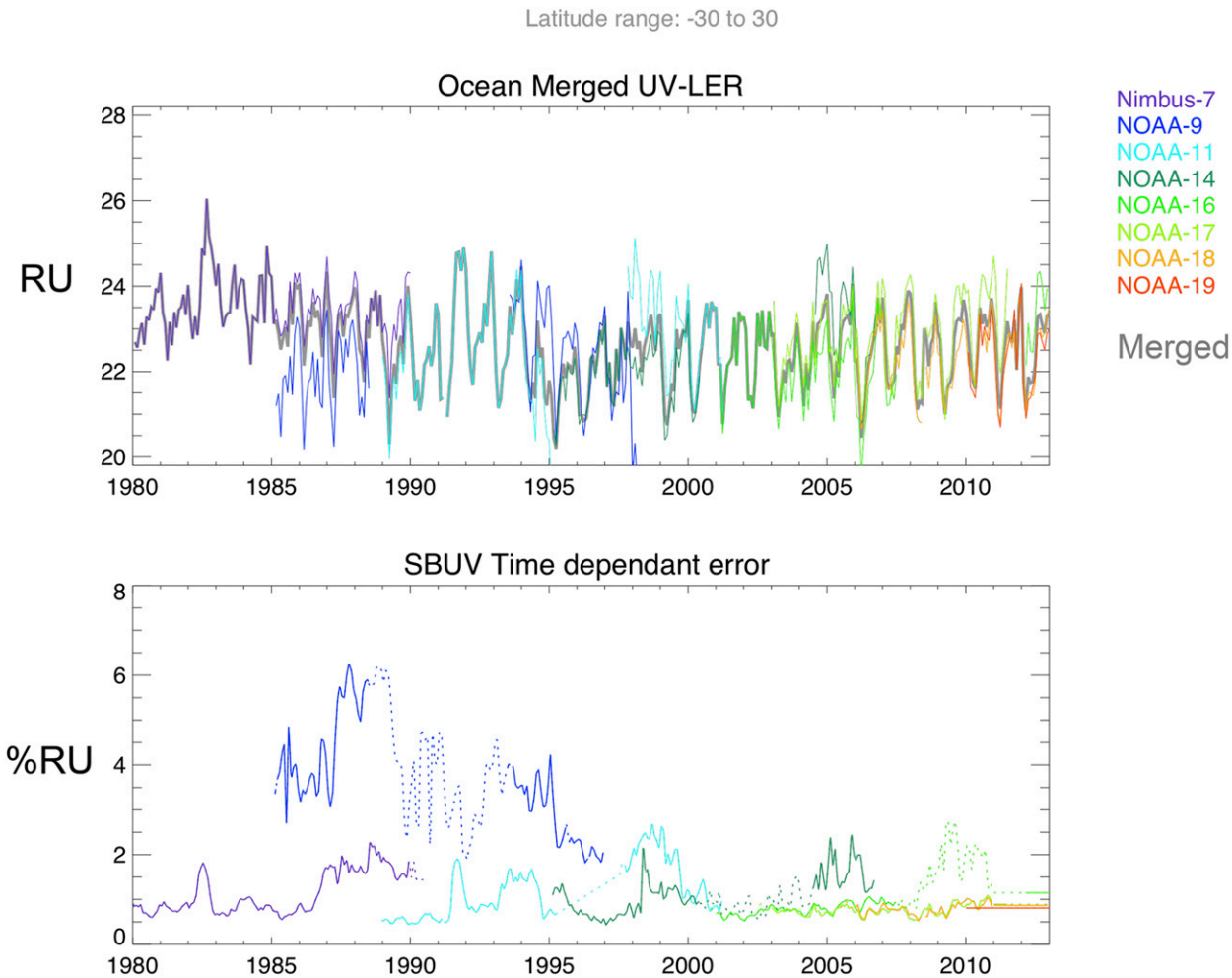

FIG. 2. (top) UV LER at 340 nm from individual SBUV and SBUV/2 instruments (different colors, see legend). Merged UV LER data record (gray). (bottom) Time-dependent errors used to inversely weight the individual SBUV/2 UV LER instruments records in terms of percent RU. Dotted lines indicate segments of data not used in the merged product.

These residuals are differences between the SBUV observed radiances and the best-fit simulated radiances from measured cross sections and radiative transfer calculations. The quality of the ozone profiles degrade with increasing solar zenith angle so the MOD only includes individual SBUV/2 instrument records when the local equator-crossing time of the orbit is between 0800 and 1600. We adopt the same criteria when constructing our merged UV LER record.

Also, when constructing our merged product, we inversely weigh each SBUV/2 instrument by its time-dependent error (Table 1) and the instrument's ozone residuals. We include the ozone residual information as an additional measure of instrument quality. The ozone residuals are relatively small when an instrument is operating optimally and the diffuser plate is being accurately monitored, but they will increase at high solar zenith angles or if there is an instrument problem. Specifically, we use residuals from ozone retrievals using the three longest wavelengths used in the ozone profile retrieval algorithm (see Fig. 21 of Deland et al. 2012). We normalize the time series of ozone residuals to the time-dependent error (Table 1) for each instrument (Fig. 2, bottom). Note the high uncertainty for *NOAA-9* and the low uncertainties of the more recent instruments. When the inversely weighted individual SBUV/2 instruments are finally merged (gray line of Fig. 2, top), the product is closer to *Nimbus-7*, even when *NOAA-9* first becomes available in 1985.

The LER dataset is gridded 2° latitude × 5° longitude and has one grid value every 10 days. Each grid value is composed of an average of 4–5 measurements. The SBUV/2 instrument field of view has a nadir footprint of 168 km ×168 km, which is equivalent to 1.5° × 1.5° at the equator. The large pixel size means that the effects of many clouds are averaged together so that the Lambertian reflection assumption is reasonable.

3. Current satellite observations of cloud radiative forcing

As mentioned in the introduction, we consider two observational records of cloud radiative forcing R_{cloud} from satellite: CERES and ISCCP FD. We construct our new record of R_{cloud} using the CERES data record and validate it with the ISSCP FD record.

a. CERES

The CERES TOA clear-sky and all-sky albedos used in our study are from daily means of the single-scanner footprint TOA fluxes from *Terra* (CERES_SSF1deg-Day-lite_Terra_Ed2.8; Wielicki et al. 1996). To generate the fluxes, the CERES measurements are combined with scene information from a higher-resolution imager such as the Visible Infrared Imaging Radiometer Suite (VIIRS) or the Moderate Resolution Imaging Spectroradiometer (MODIS). Since we are interested in radiative forcing only due to clouds, we use the difference between the clear-sky TOA albedo minus the all-sky TOA albedo. The clear-sky product only includes forcing from water vapor and surface albedo, and the all-sky product includes all forcings. The difference of these two products (clear sky − all sky), the cloud radiative forcing albedo (α_{cloud}), is largely sensitive to changes in cloud properties and amount (see lower part of Fig. 1). Note that direct and indirect aerosol effects are also included in our α_{cloud}.

We also ran our analysis using the *Aqua* data (CERES_SSF1deg-Day-lite_Aqua_Ed2.8) and see little difference in the results.

b. ISCCP FD

The ISCCP has produced a global radiative flux data product ISCCP FD from 1983 to 2009 (Zhang et al. 2004). This product employs the NASA GISS global circulation model radiative transfer code along with a host of observational datasets to produce physically consistent TOA radiative fluxes. Besides the ISCCP cloud datasets, daily profiles of temperature and humidity from NOAA, ozone from the Total Ozone Mapping Spectrometer (TOMS), and stratospheric aerosols from Stratospheric Aerosol and Gas Experiment (SAGE) are used in the radiative transfer calculation—no UV upwelling radiances were used in this product. For our purposes, we use the all-sky and clear-sky SW TOA fluxes.

4. Methodology

When clouds are present they reflect more solar radiation to space than under clear conditions, except over snow and ice. The quantity SW cloud radiative forcing R_{cloud} quantifies this effect and is calculated as clear-sky minus cloudy-sky (or all-sky) reflected radiation at the TOA. Our intent is to first transform the 34-yr, 340-nm UV LER data record to a broadband SW cloud radiative forcing albedo α_{cloud} and then to SW R_{cloud} using a set of linear equations—one equation for each latitude band and cloud optical depth range.

Using a scaling approach, we convert the UV LER product to SW α_{cloud} using 14 yr of the CERES data to produce a 34-yr "CERES like" SW α_{cloud} dataset. Besides spectral bandwidth, there are other important differences between the UV LER and the SW CERES products. All the measurements used in our UV LER record were nadir viewing. But the CERES instrument observes directional (not necessarily nadir view) radiances according to the satellite platform viewing geometry. While the UV LER assumes a Lambertian surface, the CERES albedo algorithm attempts to account for the BRDF of the earth's surface. An angular directional model (ADM) was used to convert the directional radiances to a hemispheric albedo. The appropriate ADM was chosen from a suite of 600 models based on the geotype, imager cloud property, and atmospheric structure (Wielicki et al. 1998).

Since the UV LER product is sensitive to surface snow and ice in addition to cloudiness, we remove snow- or ice-contaminated scenes based on the surface snow fraction quantity (FNSO) produced by the Modern-Era Retrospective Analysis for Research and Applications (MERRA; see appendix). For each 2° × 5° grid cell, we check if FNSO reports any snow within the cell over the appropriate 10-day period. If there is any report of snow, both the UV LER and CERES SW α_{cloud} are flagged (yellow boxes in Fig. 1). Next, we bin each 2° × 5° grid cell by surface type (land or ocean), by latitude, and by the cloud optical depth based on the ISCCP climatology. We use eight latitude bands for each hemisphere: 60°–45°, 45°–30°, 30°–15°, 15°–0°. We use four cloud optical depth bins: 0–3, 3–4.5, 4.5–6, and >6.

For the ith bin (i = 1–64), we derive a linear equation that will convert the UV LER to SW α_{cloud}. We want the 14-yr average amplitude variability in the LER CERES-like SW α_{cloud} to be of the same magnitude as those of the CERES product. We define the scaling factor a_i as the standard deviation of the amplitude anomalies (σ) of the CERES α_{cloud} divided by σ (UV LER) for the CERES period, 2000–13. The additive constant b_i is set so that the mean of the CERES-like SW α_{cloud} is equal to the actual CERES product (see yellow boxes in Fig. 1).

To obtain the 34-yr SW α_{cloud}, we individually process each gridded 2° latitude × 5° longitude 10-day UV LER value. We find its appropriate cloud optical depth (OD) bin, its latitude band bin, and its ocean–land surface condition

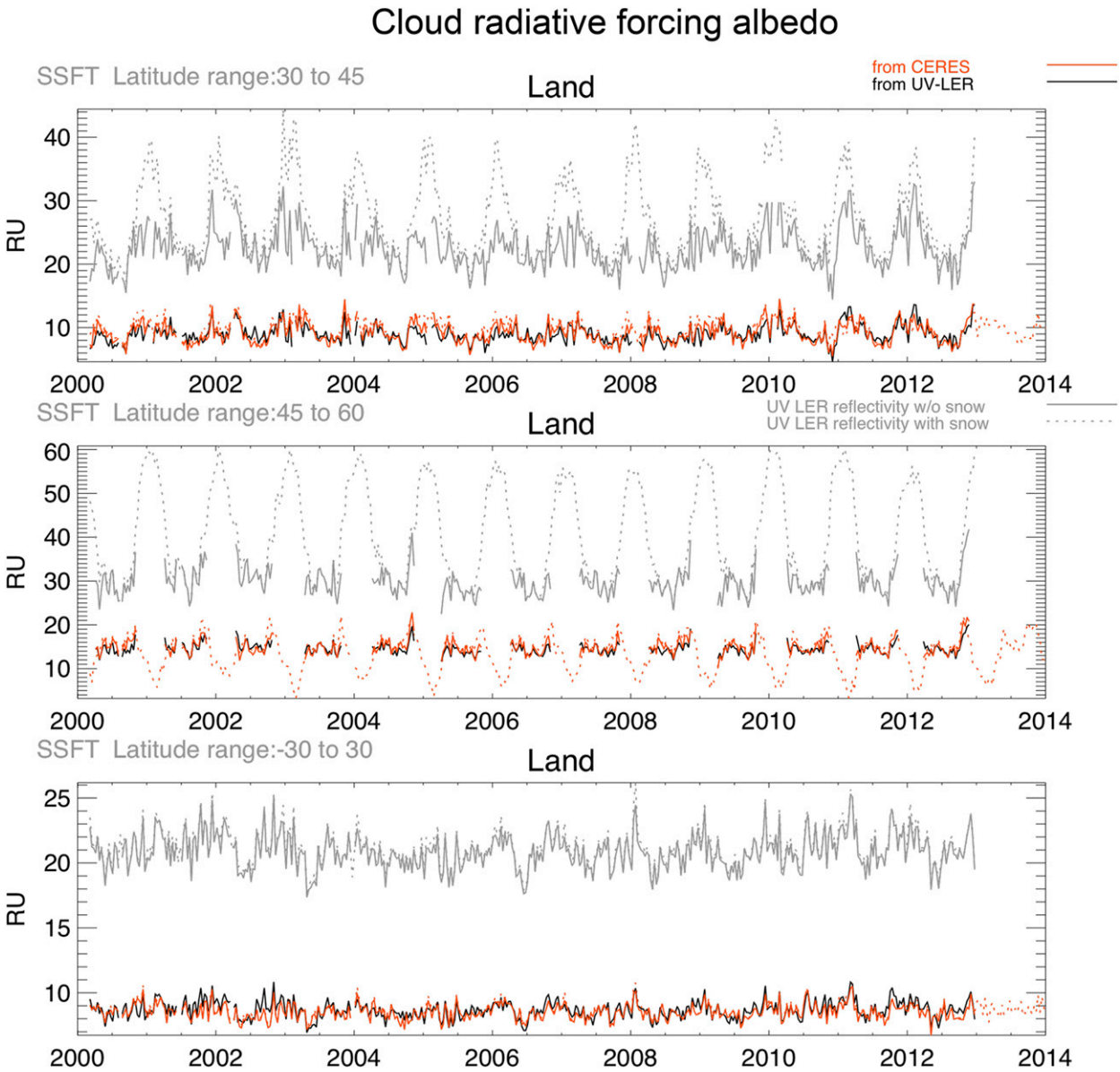

FIG. 3. Comparison of 10-day averaged CERES hemispheric SW α_{cloud} (red) and our derived CERES-like SW α_{cloud} derived from UV LER (black) for (top)–(bottom) specified latitudinal bands over land. Also shown are LER from observed upwelling UV radiances (gray). An albedo of 1 = 100 RU. Solid line traces do not include snow-filled grids. Dotted line traces include the snow-flagged grid boxes, but they are not used in the analysis.

and then apply the appropriate scaling factor (a_i) and additive constant (b_i). To calculate SW R_{cloud}, we multiply SW α_{cloud} by the TOA incident downward SW flux. Our downward SW flux is based on gridded values of the MERRA downward incident solar radiation (SWTDN). We incorporate total solar irradiance (TSI) observations by adjusting the MERRA values so that the annualized global mean values agree with annual TSI reconstruction values from the Solar Radiation and Climate Experiment (SORCE; Krivova et al. 2010; Ball et al. 2012).

5. Results

a. *Compare UV-derived CERES-like SW α_{cloud} with CERES*

Figure 3 shows the UV LER (gray trace), the CERES SW α_{cloud} (red), and our CERES-like SW α_{cloud} (black) for three latitude bands over land. Poleward of 30°N (top two panels), the two albedos track well over snow- or ice-free surfaces. The UV LER dotted lines show averages that include the snowy grid cells. As expected, inclusion

TABLE 2. Statistics from linear scaling of UV LER to the CERES-like SW α_{cloud} by bin. Corr (r) is the correlation of monthly values CERES SW α_{cloud} with UV LER. Slope (a_i) is the scaling factor converting UV LER to CERES-like SW α_{cloud}. RMS scaling diff is the RMS of (CERES minus CERES-like SW α_{cloud}) for all 2° × 5° grid cells in bin (1-sigma). An insufficient sample size is denoted with an em dash.

Cloud OD	Latitude band (°)	Corr (r)	Slope (a_i)	CERES-like α_{cloud} (RU)	RMS scaling diff 2° × 5° grid cell
			Ocean		
0–3	From −60 to −55	—	—	—	—
3–4.5	From −60 to −55	—	—	—	—
4.5–6	From −60 to −55	0.30	0.36	27.04	5.52
>6	From −60 to −55	−0.15	0.61	25.62	13.38
0–3	From −55 to −40	0.56	0.39	15.17	4.79
3–4.5	From −55 to −40	0.48	0.35	20.81	4.35
4.5–6	From −55 to −40	0.43	0.35	24.29	4.44
>6	From −55 to −40	0.32	0.40	27.80	5.58
0–3	From −40 to −25	0.58	0.40	12.55	4.49
3–4.5	From −40 to −25	0.57	0.42	16.28	4.78
4.5–6	From −40 to −25	0.49	0.35	20.39	4.31
>6	From −40 to −25	—	—	—	—
0–3	From −25 to 25	0.73	0.50	9.43	4.16
3–4.5	From −25 to 25	0.71	0.49	11.99	4.49
4.5–6	From −25 to 25	0.69	0.50	15.72	4.60
>6	From −25 to 25	0.63	0.59	18.29	5.74
0–3	From 25 to 40	0.66	0.51	10.57	4.54
3–4.5	From 25 to 40	0.68	0.51	14.81	5.27
4.5–6	From 25 to 40	0.66	0.47	19.80	5.33
>6	From 25 to 40	0.63	0.43	24.24	5.62
0–3	From 40 to 55	—	—	—	—
3–4.5	From 40 to 55	0.64	0.44	18.37	5.22
4.5–6	From 40 to 55	0.54	0.41	23.86	5.15
>6	From 40 to 55	0.52	0.37	26.67	4.55
0–3	From 55 to 60	—	—	—	—
3–4.5	From 55 to 60	−0.16	0.37	16.78	11.15
4.5–6	From 55 to 60	0.15	0.53	22.27	9.85
>6	From 55 to 60	0.09	0.44	26.08	8.45
			Land		
0–3	From −60 to −55	—	—	—	—
3–4.5	From −60 to −55	—	—	—	—
4.5–6	From −60 to −55	—	—	—	—
>6	From −60 to −55	—	—	—	—
0–3	From −55 to −40	0.58	0.35	9.52	3.90
3–4.5	From −55 to −40	—	—	—	—
4.5–6	From −55 to −40	0.57	0.42	19.62	5.74
>6	From −55 to −40	—	—	—	—
0–3	From −40 to −25	0.61	0.36	7.02	4.06
3–4.5	From −40 to −25	0.60	0.37	11.36	5.04
4.5–6	From −40 to −25	—	—	—	—
>6	From −40 to −25	—	—	—	—
0–3	From −25 to 25	0.78	0.48	5.47	3.92
3–4.5	From −25 to 25	0.77	0.52	10.51	4.86
4.5–6	From −25 to 25	0.76	0.55	14.27	5.45
>6	From −25 to 25	0.77	0.54	18.48	5.56
0–3	From 25 to 40	0.70	0.42	4.49	3.69
3–4.5	From 25 to 40	0.73	0.50	7.11	5.13
4.5–6	From 25 to 40	0.61	0.44	17.20	6.55
>6	From 25 to 40	0.67	0.43	21.55	6.40
0–3	From 40 to 55	0.61	0.40	9.93	4.79
3–4.5	From 40 to 55	0.64	0.44	12.92	5.94
4.5–6	From 40 to 55	0.64	0.43	15.77	5.95
>6	From 40 to 55	0.60	0.43	20.61	5.73
0–3	From 55 to 60	0.54	0.37	18.79	5.17
3–4.5	From 55 to 60	0.48	0.38	16.95	6.13
4.5–6	From 55 to 60	0.59	0.44	19.07	6.63
>6	From 55 to 60	0.38	0.49	24.86	8.63

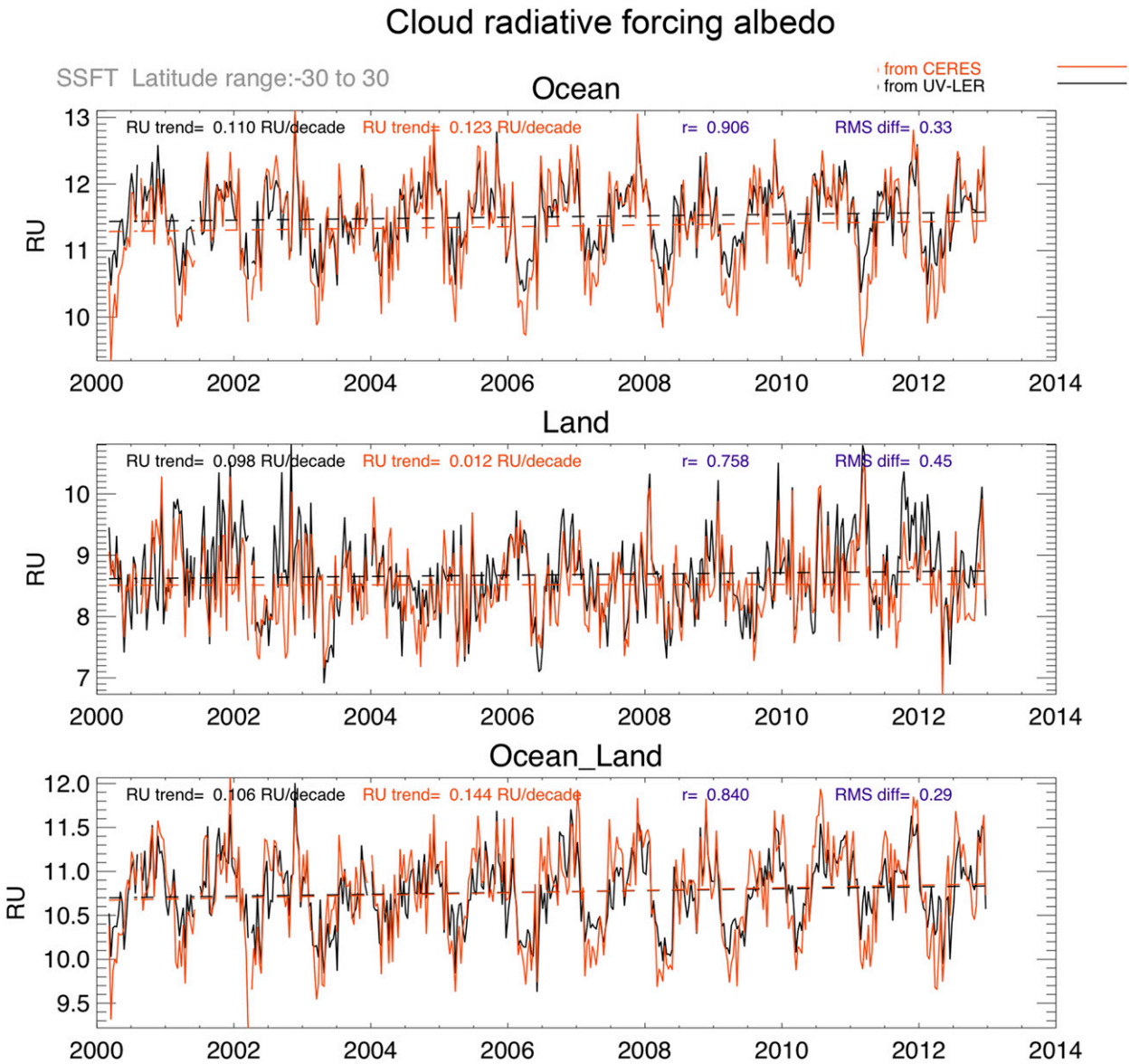

FIG. 4. Comparison of CERES α_{cloud} (red) and our derived CERES-like α_{cloud} derived from UV LER (black) for 30°S–30°N latitudinal band over (top) ocean, (middle) land, and (bottom) their differences. Trends, correlation coefficients, and RMS differences are shown at the tops of each panel.

of snowy cells shows a strong seasonal cycle with high values in the winter. Also note that the UV LER is about twice as sensitive to changes in cloudiness compared with the CERES α_{cloud}.

This simple scaling approach is only possible because of the good linear relationship between the UV LER and CERES SW α_{cloud}, shown by the good correlations in Table 2. Only at the higher latitudes does this linear relationship break down. Still, the root-mean-square (RMS) of [CERES α_{cloud} − CERES-like α_{cloud}] for any given 2° × 5° grid cell can be quite large (4–10 RU; see the RMS scaling difference column of Table 2).

Depending on the latitude, cloud OD, and surface (ocean or land), we apply the same scaling factor over the entire length of the 34-yr UV LER record. While the absolute values of our derived CERES-like SW α_{cloud} will depend on the CERES SW α_{cloud}, short-term trends and anomalies will not. Instead, they will be dependent only on the UV LER record. A time series of the CERES SW α_{cloud} compared with our CERES-like for 30°S–30°N shows good visual correlation over both land and ocean (Fig. 4). Over ocean CERES-like SW α_{cloud} explains over 82% ($r = 0.91$) of the variance in the CERES product, although much of this is seasonal driven. Over

TABLE 3. Trends and uncertainties of SW α_{cloud} for 2000–13.

Latitude band (°)	SW α_{cloud} trends uncertainties[a]		SW α_{cloud} trends[b] (RU decade^{-1})			
	Scaling difference	T.D. error	CERES	2-sigma error	CERES-like	2-sigma error
			Ocean			
From −60 to −45	1.62	0.30	0.31	0.55	0.04	0.43
From −45 to −30	1.12	0.21	−0.07	0.55	−0.17	0.30
From −30 to −15	1.31	0.19	0.17	0.55	0.11	0.36
From −15 to 0	1.60	0.19	−0.19	0.55	−0.12	0.43
From 0 to 15	1.57	0.21	0.17	0.55	0.12	0.42
From 15 to 30	1.43	0.18	0.41	0.55	0.39	0.38
From 30 to 45	2.86	0.25	−0.02	0.55	−0.04	0.73
From 45 to 60	1.90	0.31	−0.34	0.55	−0.07	0.50
From −30 to 30	0.88	0.19	0.12	0.55	0.11	0.26
From −60 to 60	0.74	0.22	0.17	0.55	0.09	0.22
			Land			
From −60 to −45	3.54	0.31	−0.38	0.61	−0.59	1.01
From −45 to −30	2.60	0.15	−0.64	0.55	−0.62	0.67
From −30 to −15	2.60	0.15	−0.03	0.55	0.05	0.67
From −15 to 0	3.24	0.25	−0.29	0.55	−0.01	0.83
From 0 to 15	3.04	0.19	0.24	0.55	0.17	0.78
From 15 to 30	1.83	0.14	0.01	0.55	0.17	0.48
From 30 to 45	1.92	0.21	0.13	0.55	0.42	0.51
From 45 to 60	1.43	0.30	0.06	0.68	0.08	0.47
From −30 to 30	0.88	0.18	0.01	0.55	0.10	0.26
From −60 to 60	0.78	0.21	0.03	0.55	0.20	0.23

[a] Contributions to the CERES-like SW α_{cloud} uncertainty. Scaling differences are differences between the CERES values and the CERES-like values. The time-dependent errors are based on those reported for each SBUV/2 instrument. Both are 1-sigma uncertainties in terms of RU.

[b] Trends of SW α_{cloud} in RU per decade. The CERES column is from CERES-*Terra* observations; its 2-sigma error is derived from the differences between the *Terra* and *Aqua* instruments when they temporally overlap. The CERES-like column is our α_{cloud} product derived from the UV LER reflectivity; its 2-sigma error is derived from the time-dependent and the scaling differences. (see uncertainty analysis section in appendix).

land the correlation has degraded (r = 0.76) and our CERES-like SW α_{cloud} only explains about 57% of the variance of the actual CERES product.

Table 3 shows the scaling differences and time-dependent error (second and third columns) that both contribute to the uncertainty in the CERES-like SW α_{cloud} product. Of these, the scaling difference dominates (see uncertainty analysis section in the appendix). Columns 4–7 compare the CERES and CERES-like trends and associated 2σ uncertainties and are discussed in the next section.

b. Compare CERES-like R_{cloud} with CERES

To test our scaling approach, we compare monthly anomalies of our CERES-like R_{cloud} with CERES over the period 2000–13. Figure 5 shows comparisons for tropical band 30°S–30°N. Monthly anomalies are calculated by averaging all values for each month of the 34 yr (there are 34 Januaries from 1980 to 2013, so N = 34). The anomaly is the actual value minus the average for the appropriate calendar month. Both the CERES *Aqua* and *Terra* traces almost always lie within the 2-sigma uncertainty of our CERES-like values shown by the gray shading. Over the tropical band, the new CERES-like record captures about 58% (r = 0.76) of the explained variance of the CERES record based on the correlation over ocean and land (Fig. 5). Over narrower latitude bands, the explained variance can reach 83% (r = 0.91; see sixth column in Table 4). Although there is also good agreement between the CERES-like and CERES records over the broad 60°S–60°N band (r = 0.76 over ocean), the reduced correlations above 55° latitude (Tables 3 and 4) lend higher uncertainty to any local trends seen at high latitudes.

Zonal mean trends of R_{cloud} over the 2000–13 period are shown in Fig. 6 by the red (CERES-*Terra*) and black (CERES-like) traces; the error bars are 2-sigma, 95% confidence level uncertainties in the trends. These trends are also listed in columns 4–7 of Table 3. The uncertainties in the R_{cloud} values contribute to the uncertainties in the trends. The narrower latitude bands (left-hand side of Fig. 6, connected by lines) show similar latitudinal patterns. Some latitude bands show similar

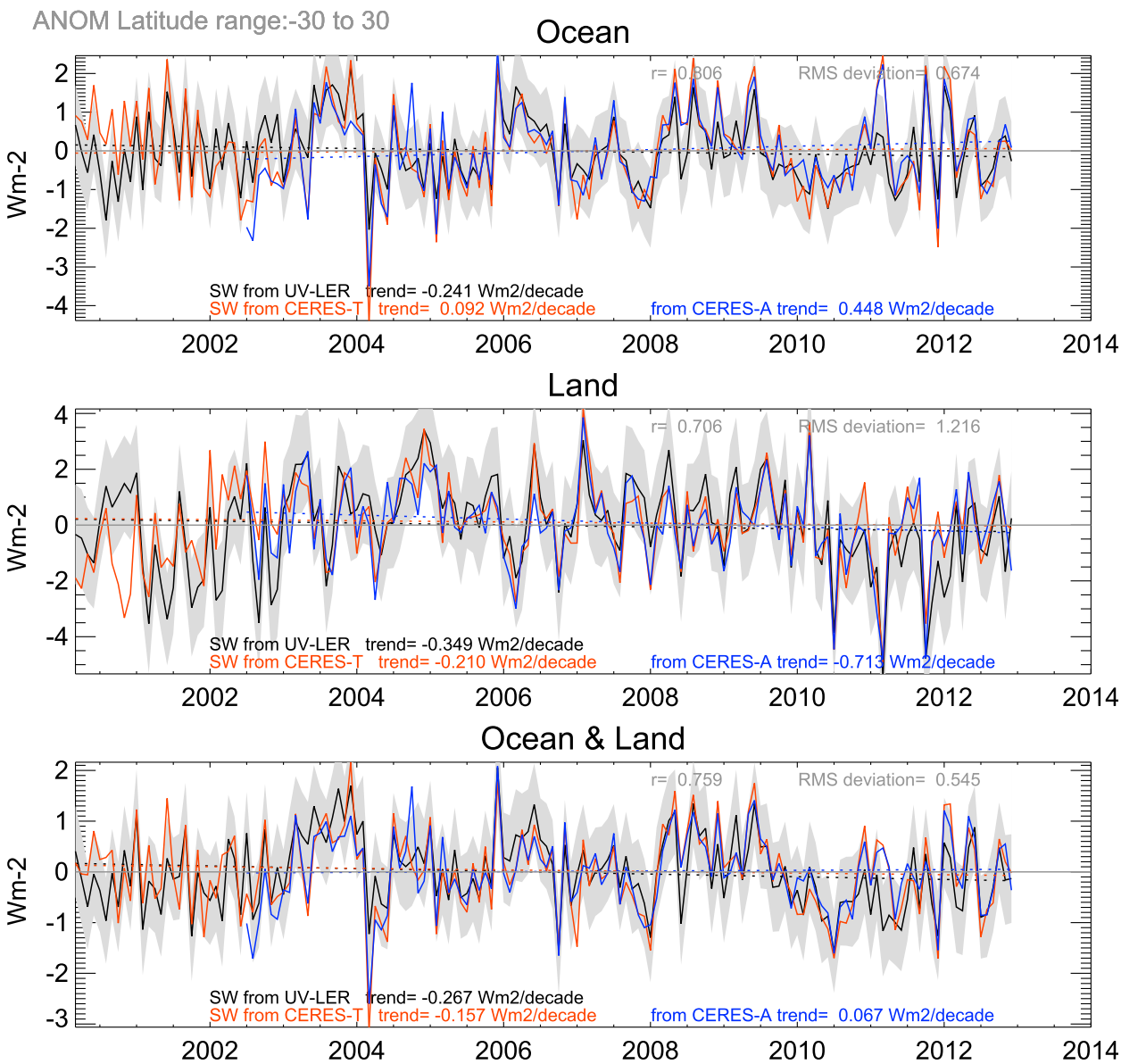

FIG. 5. Comparison of monthly anomalies of CERES-like SW R_{cloud} from UV LER (black) with the CERES-*Terra* (red) and CERES-*Aqua* (blue) cloud radiative forcing for 30°S–30°N for the period 2000–13 over (top) ocean, (middle) land, and (bottom) their sums. Shaded area is the 2-sigma uncertainty for the CERES-like SW R_{cloud}. Trends are shown at the bottoms of each panel, and correlation coefficients and RMS differences at the top.

trends that are statistically different than zero at 95% confidence level: ocean (15°–30°N) and land (45°–60°N). Other bands show poorer agreement between the CERES-*Terra* and CERES-like traces. The unconnected dots (right-hand side of Fig. 6) show that the trend uncertainties overlap for both the tropical 30°S–30°N and the broad 60°S–60°N latitude bands. This suggests that over the 2000–13 period, the trends in CERES R_{cloud} are consistent with trends in the CERES-like record and the UV LER record.

The uncertainty range for the long-term trends (1980–2013) in CERES-like R_{cloud} is significantly reduced (blue dots in Fig. 6). All ocean, and most land, latitudinal bands show statistically significant (95% confidence level) positive R_{cloud} forcing. The strongest trend of $+1.3\,\mathrm{W\,m^{-2}\,decade^{-1}}$ occurs over ocean in the narrow band (15°S–0°). At the wider latitudinal bands (30°S–30°N and 60°S–60°N) the $+0.5\,\mathrm{W\,m^{-2}\,decade^{-1}}$ R_{cloud} trend is mainly driven by changes over ocean. All plotted values for Fig. 6 are listed in Table 4.

TABLE 4. Trends and uncertainties of SW R_{cloud}. For 2000–13 comparison of CERES and CERES-like, the 2-sigma error for CERES is derived from differences between the *Terra* and *Aqua* instruments. The 2-sigma error for CERES-like includes contributions from the scaling difference, the time-dependent error, and the estimated 1-RU instrument noise (see uncertainty analysis section in appendix). Tabular values from Fig. 6.

	SW R_{cloud} trend 2000–13 (W m^{-2} decade^{-1})				SW R_{cloud} trend 1980–2013 (W m^{-2} decade^{-1})		
Latitude band (°)	CERES	2-sigma error	CERES-like	2-sigma error	Corr	CERES-like	2-sigma error
			Ocean				
From −60 to −45	−0.27	0.09	0.02	0.15	0.78	0.20	0.04
From −45 to −30	−0.05	0.11	0.44	0.24	0.69	0.10	0.06
From −30 to −15	0.07	0.19	−0.36	0.36	0.83	0.25	0.09
From −15 to 0	1.65	0.20	0.58	0.39	0.83	1.35	0.09
From 0 to 15	0.35	0.17	−0.11	0.46	0.91	0.61	0.11
From 15 to 30	−1.49	0.15	−1.31	0.40	0.81	0.10	0.10
From 30 to 45	0.22	0.13	0.17	0.41	0.82	0.31	0.10
From 45 to 60	0.10	0.12	0.09	0.31	0.64	0.23	0.07
From −30 to 30	0.09	0.11	−0.24	0.22	0.81	0.73	0.05
From −60 to 60	−0.12	0.07	−0.11	0.15	0.72	0.51	0.04
			Land				
From −60 to −45	0.64	0.97	0.37	2.40	0.72	0.14	0.61
From −45 to −30	1.72	0.48	2.23	0.95	0.79	0.70	0.24
From −30 to −15	−0.17	0.34	0.37	0.66	0.78	0.42	0.16
From −15 to 0	1.52	0.59	0.30	0.90	0.56	0.48	0.22
From 0 to 15	−0.47	0.48	−0.67	0.81	0.78	0.06	0.20
From 15 to 30	0.65	0.22	−0.58	0.50	0.77	−0.21	0.12
From 30 to 45	1.41	0.19	0.43	0.49	0.76	0.37	0.12
From 45 to 60	1.21	0.18	1.35	0.56	0.70	0.70	0.14
From −30 to 30	−0.21	0.25	−0.35	0.37	0.71	0.07	0.09
From −60 to 60	0.18	0.17	−0.03	0.28	0.66	0.22	0.07
			Ocean and land				
From −60 to −45	−0.26	0.09	0.02	0.15	0.78	0.20	0.04
From −45 to −30	0.07	0.11	0.57	0.23	0.72	0.14	0.06
From −30 to −15	−0.16	0.17	−0.19	0.31	0.84	0.29	0.08
From −15 to 0	1.08	0.22	0.52	0.36	0.82	1.15	0.09
From 0 to 15	0.06	0.18	−0.24	0.40	0.87	0.48	0.10
From 15 to 30	−0.71	0.13	−1.05	0.31	0.78	−0.01	0.08
From 30 to 45	0.56	0.11	0.26	0.31	0.85	0.34	0.08
From 45 to 60	0.49	0.10	0.38	0.26	0.82	0.30	0.06
From −30 to 30	−0.16	0.10	−0.27	0.19	0.76	0.56	0.05
From −60 to 60	−0.10	0.07	−0.07	0.13	0.77	0.44	0.03

c. *Validation of CERES-like R_{cloud} using ISCCP FD observations*

The comparison of our CERES-like R_{cloud} record with ISCCP FD is mixed. At low latitudes (Fig. 7a), R_{cloud} from ISCCP FD (green) and our CERES-like product (black) both capture the gradual increase in R_{cloud} (1987–91), the rapid decrease from the Mount Pinatubo volcanic eruption in 1991, and the recovery afterward. Both show the dramatic decrease in R_{cloud} driven by the increased convection from the 1998 El Niño event and often match anomalous temporal features thereafter. Over ocean, the correlation (r = 0.747) is respectable, but over land there is poor agreement. At midlatitudes (30°–45°N, Fig. 7b) temporal features are similar for both datasets and the correlations are still respectable (r = 0.681 for ocean). Poleward of 45° there is little agreement between the datasets (not shown). For consistency, the tropical band 30°S–30°N is also shown (Fig. 7c).

6. Discussion

We present a 34-yr record of a shortwave cloud radiative forcing based on an existing UV LER record. While this new cloud radiative forcing record is scaled to match the CERES shortwave cloud radiative forcing, the underlying overall trend of the new data record (CERES like) is solely based on the UV LER record. The good agreement between trends and anomalies of the two records, when they temporally overlap (2000–13), supports using this new dataset for climate studies.

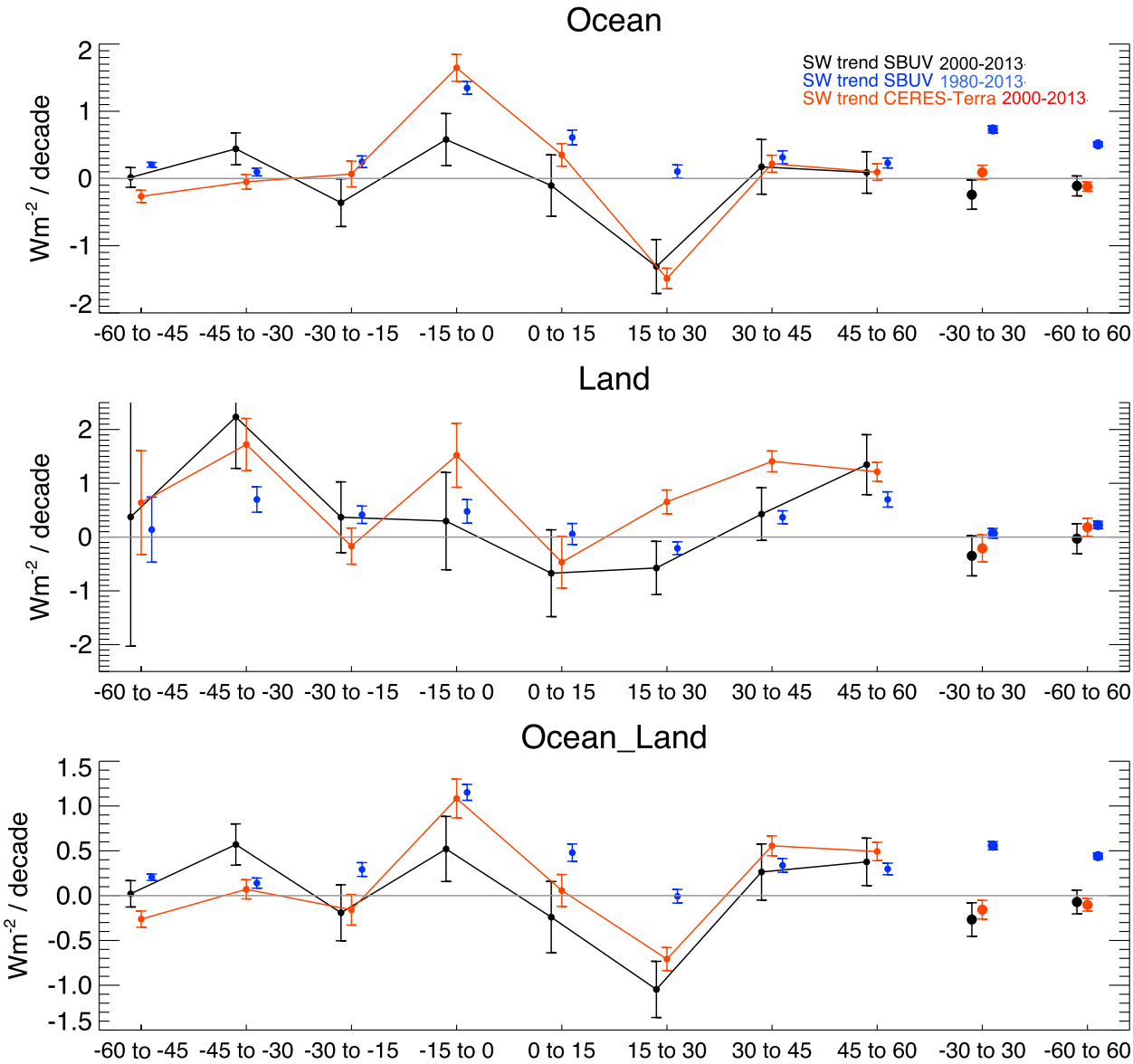

FIG. 6. Zonal mean trends of the monthly anomalies of SW R_{cloud} from UV LER (black) and from CERES-*Terra* (red) for the period 2000–13 over (top) ocean, (middle) land, and (bottom) their differences. Longer term trends for the period 1980–2013 from SW R_{cloud} from UV LER (blue dots only) are also shown. Error bars span 2-sigma uncertainty in the trends. Values are in listed in Table 4.

We have confidence in the temporal progression in CERES-like R_{cloud} over the tropical 30°S–30°N band (Fig. 7c): an increase from 1980 to 1995 followed by a decrease to 2013. The low R_{cloud} reported in the early 1980s are from higher UV LER anomalies measured by *Nimbus-7*. This instrument was in a stable orbit with an equator-crossing time within 1 h of local noon (Fig. 7; DeLand et al. 2012); this minimized cloud diurnal cycle errors. Moreover, the diffuser plate darkening was well characterized by the pair justification method (see section 2a) so that the reported time-dependent error was as low as the more recent SBUV/2 instruments (Fig. 1). There are issues with the UV LER record from 1987 to 1989 when the quality degraded; *Nimbus-7* had issues with its electronics and *NOAA-9* has serious diffuser plate issues. But with the launch of *NOAA-11* and thereafter, there has almost always been an SBUV/2 instrument with low time-dependent errors and tight ozone residuals.

A caveat of this study is the stability of the scaling factor used to convert the UV LER to a CERES-like SW α_{cloud}. As discussed above, our scaling factor is

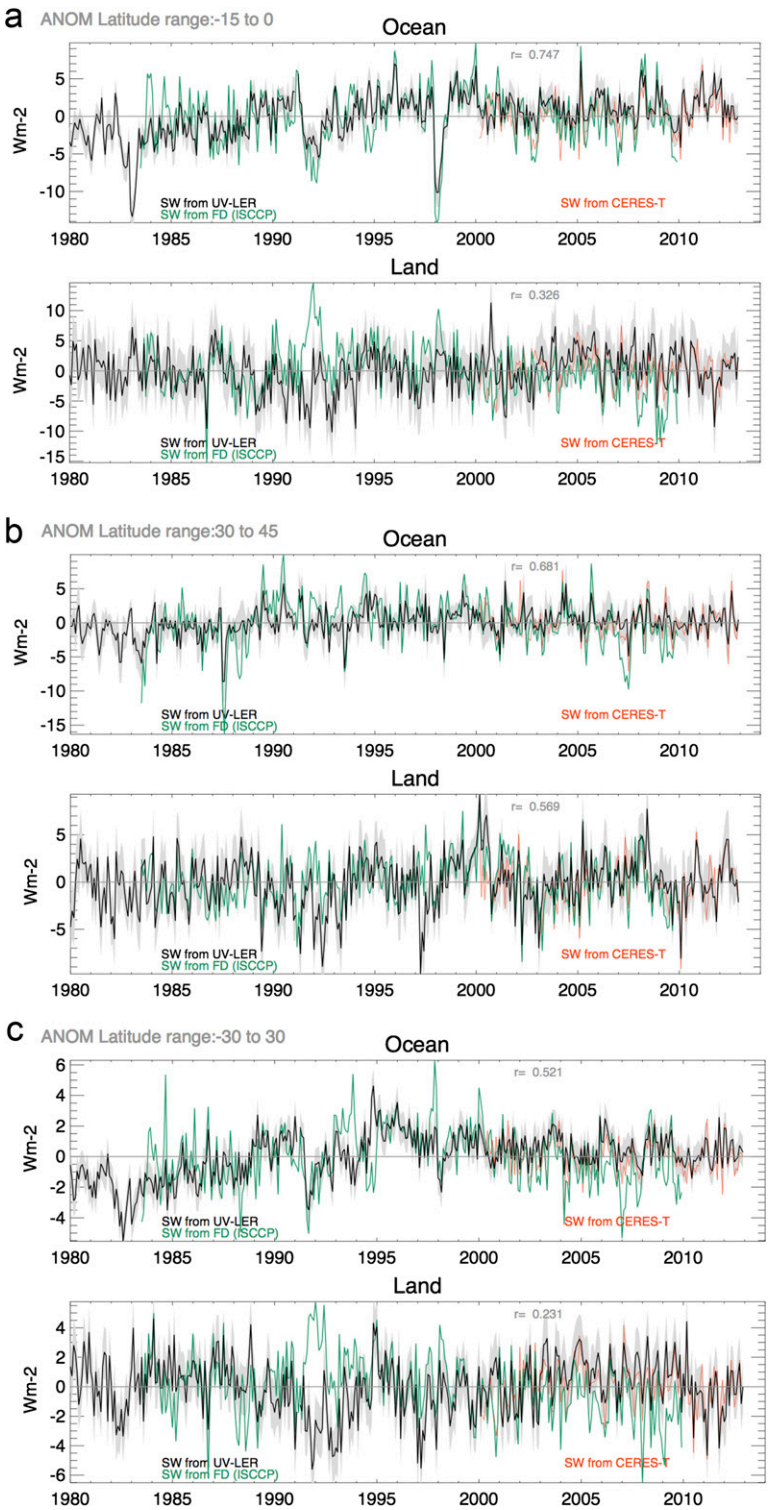

FIG. 7. Comparison of monthly anomalies of CERES-like SW R_{cloud} from UV LER (black) with ISCCP FD (green) and with CERES-*Terra* (red) for (a) 15°S–0°, (b) 30°–45°N, and (c) 30°S–30°N. Shaded area is the 2-sigma uncertainty for the CERES-like SW R_{cloud}. Correlations shown at the top of each panel are for CERES-like SW R_{cloud} and ISCCP FD from 1983 to 2009.

σ(CERES α_{cloud})/σ(UV LER), where σ is the standard deviation of the monthly anomalies. Depending on the latitude band, cloud OD, and surface type, the factor ranges between 0.35 and 0.55 (Table 2). The high correlation and trends between CERES and CERES-like α_{cloud} (Fig. 4) suggest the scaling factors are stable with time, but our conclusions could change if this is not the case. One mechanism that might change the scaling factors is the cloud vertical extent. At tropical and midlatitudes the TOA reflectance is related to cloud amount, but at high solar zenith angles nadir reflectance is also sensitive to the slope of the cloud top and the cloud sides (the cloud vertical extent; Loeb et al. 1997). This may explain the low correlations between CERES SW α_{cloud} versus UV LER at latitudes poleward of 55°($r < 0.3$ over ocean) and the better correlations at tropical latitudes ($r \sim 0.7$ over ocean, Table 2). There may be other unknown mechanisms that change the scaling factors. Our reported trends and conclusions assume that if the vertical extent of clouds has changed over the 34 yr, its impact on our scaling factors is limited to the highest latitudes. Otherwise, our α_{cloud} and R_{cloud} derived from LER will be in error. Future investigation might study how cloud height and vertical extent impact the measured radiances.

An additional source of error in our reported trends in R_{cloud} is that the 340-nm upwelling measurements are sensitive to aerosol amount and type. Any decadal changes in aerosols loading (1980–2014) will impact our results, but we expect this issue to be limited to strong aerosol source regions.

Table 4 shows a SW R_{cloud} decadal trend over ocean and land from 60°S to 60°N of $+0.43 \pm 0.032\,\mathrm{W\,m^{-2}}$. This is equivalent to $+1.47 \pm 0.11$ over the 34-yr period of the UV LER dataset. Using the same UV LER dataset as we use here, Herman et al. (2013) conclude that changes in clouds, aerosols, and surface reflectivity lead to an increased SW absorption of $2.35\,\mathrm{W\,m^{-2}}$ based on a perturbation to an atmospheric energy balance model given by Trenberth et al. (2009). Granted, our study does not include surface reflectivity changes due to snow, but including this effect only bumps our absorption to $1.55\,\mathrm{W\,m^{-2}}$. The main difference between our 1.47 and their $2.35\,\mathrm{W\,m^{-2}}$ is likely from the reduced scaling factor used for our study.

Acknowledgments. This research is supported by the NASA MEaSUREs Project. We appreciate helpful discussions with Matthew Deland, Stacey Frith, P. K. Bhartia, Mathew Zelinka, and Andrew Dessler. We also appreciate the comments of two anonymous reviewers.

APPENDIX

MERRA

The Global Modeling and Assimilation Office at the NASA Goddard Space Flight Center has used the Goddard Earth Observing System Model, version 5 (GEOS-5), atmospheric data assimilation system to synthesize the observations collected over the satellite era (since 1979) to produce 36 yr of meteorological analyses that are consistent over time because it uses a fixed assimilation system (Rienecker et al. 2011). This historical reprocessing is called MERRA. The MERRA downward incident solar radiation (SWTDN) does not account for the $0.25\,\mathrm{W\,m^{-2}}$ variability over an 11-yr solar cycle. We modified the MERRA SWTDN product to account for the slight variation of the solar cycle. This modification has almost no impact on our results.

The MERRA FNSO is based on the GEOS-5 snow parameterization and the assimilation of observed atmospheric state (e.g., precipitation and surface temperatures). No satellite information is used in this product.

Uncertainty analysis

Since there is no validated SW α_{cloud} dataset for comparison, it is difficult to explicitly determine its accuracy. However, we can estimate a precision uncertainty based on three contributions listed below. We assume that these contributions are independent, so we calculate the total error as the square root of the sum of the squares of these three contributions (see CERES-like 2-sigma error columns of Tables 3 and 4). But these contributions may in fact be correlated, resulting in overestimated uncertainties.

1) A 1-RU uncertainty estimate accounts for SBUV/2 sensor noise for the 34-yr record. It is the standard deviation of the normalized summertime 340-nm LER from the Antarctic Plateau for the entire 34-yr record (see Fig. 1; Herman et al. 2013).
2) The UV LER record is a composite of eight different UV sensors, each with a single time-dependent error. This error is the square root of the sum of independent contributions to the overall instrument error that will vary over the life of each instrument. As mentioned earlier, a significant source of error is from the darkening of the diffuser plate with time. Additional contributions are goniometry (related to the angle of the diffuser plate) and the inter-range ratio (errors estimated from overlaps in the three different ranges of the photo multiplier tube). This time-dependent error is shown in columns 2 and 3 of Table 3.
3) The dominant contribution to the precision uncertainty is the conversion of the UV LER to SW α_{cloud} for each

cloud OD–latitude band bin. For each latitude band, we compare averages of our CERES-like SW α_{cloud} with the actual CERES value. This scaling difference is shown in the first column Table 3. This difference includes (i) differences between our simple Lambertian assumption of the earth/cloud surface and the more complex BRDF treatment in the CERES algorithms, (ii) errors in our treatment of the diurnal cloud cycle, and (iii) our inability to account for changes in nadir radiances with cloud height changes at conditions of high solar zenith angle.

REFERENCES

Ball, W. T., Y. C. Unruh, N. A. Krivova, S. Solanki, T. Wenzler, D. J. Mortlock, and A. H. Jaffe, 2012: Reconstruction of total solar irradiance 1974–2009. *Astron. Astrophys.*, **541**, A27, doi:10.1051/0004-6361/201118702.

Bhartia, P. K., R. D. McPeters, L. E. Flynn, S. Taylor, N. A. Kramarova, S. Frith, B. Fisher, and M. DeLand, 2013: Solar Backscatter UV (SBUV) total ozone and profile algorithm. *Atmos. Meas. Tech.*, **6**, 2533–2548, doi:10.5194/amt-6-2533-2013.

DeLand, M. T., R. P. Cebula, L.-K. Huang, S. L. Taylor, R. S. Stolarski, and R. D. McPeters, 2001: Observations of hysteresis in backscattered ultraviolet ozone data. *J. Atmos. Oceanic Technol.*, **18**, 914–924, doi:10.1175/1520-0426(2001)018<0914:OOHIBU>2.0.CO;2.

——, S. L. Taylor, L. K. Huang, and B. L. Fisher, 2012: Calibration of the SBUV version 8.6 ozone data product. *Atmos. Meas. Tech. Discuss.*, **5**, 5151–5203, doi:10.5194/amtd-5-5151-2012.

Herman, J. R., and E. A. Celarier, 1997: Earth surface reflectivity climatology at 340–380 nm from TOMS data. *J. Geophys. Res.*, **102**, 28 003–28 011, doi:10.1029/97JD02074.

——, R. Hudson, R. McPeters, R. Stolarski, Z. Ahmad, X.-Y. Gu, S. Taylor, and C. Wellemeyer, 1991: A new self-calibration method applied to TOMS and SBUV backscattered ultraviolet data to determine long-term global ozone change. *J. Geophys. Res.*, **96**, 7531–7545, doi:10.1029/90JD02662.

——, and Coauthors, 2013: A net decrease in the Earth's cloud plus aerosol reflectivity during the past 33 yr (1979–2011) and increased solar heating at the surface. *Atmos. Chem. Phys.*, **13**, 8505–8524, doi:10.5194/acp-13-8505-2013.

Hilsenrath, E., R. P. Cebula, M. T. DeLand, K. Laamann, S. Taylor, C. Wellemeyer, and P. K. Bhartia, 1995: Calibration of the NOAA 11 SBUV/2 ozone data set from 1989 to 1993 using in-flight calibration data and SSBUV. *J. Geophys. Res.*, **100**, 1351–1366, doi:10.1029/94JD02611.

Huang, L.-K., R. P. Cebula, S. L. Taylor, M. T. DeLand, R. D. McPeters, and R. S. Stolarski, 2003: Determination of NOAA-11 SBUV/2 radiance sensitivity drift based on measurements of polar ice cap radiance. *Int. J. Remote Sens.*, **24**, 305–314, doi:10.1080/01431160304978.

Jaross, G., and J. Warner, 2008: Use of Antarctica for validating reflected solar radiation measured by satellite sensors. *J. Geophys. Res.*, **113**, D16S34, doi:10.1029/2007JD008835.

Krivova, N. A., L. E. A. Vieira, and S. K. Solanki, 2010: Reconstruction of solar spectral irradiance since the Maunder minimum. *J. Geophys. Res.*, **115**, A12112, doi:10.1029/2010JA015431.

Labow, G. J., J. R. Herman, L.-K. Huang, S. A. Lloyd, M. T. DeLand, W. Qin, J. Mao, and D. E. Larko, 2011: Diurnal variation of 340nm Lambertian equivalent reflectivity due to clouds and aerosols over land and oceans. *J. Geophys. Res.*, **116**, D11202, doi:10.1029/2010JD014980.

Loeb, N. G., T. Várnai, and R. Davies, 1997: Effect of cloud inhomogeneities on the solar zenith angle dependence of nadir reflectance. *J. Geophys. Res.*, **102**, 9387–9395, doi:10.1029/96JD03719.

Rienecker, M. M., and Coauthors, 2011: MERRA: NASA's Modern-Era Retrospective Analysis for Research and Applications. *J. Climate*, **24**, 3624–3648, doi:10.1175/JCLI-D-11-00015.1.

Trenberth, K. E., J. T. Fasullo, and J. Kiehl, 2009: Earth's global energy budget. *Bull. Amer. Meteor. Soc.*, **90**, 311–324, doi:10.1175/2008BAMS2634.1.

Weiss, H., R. P. Cebula, K. Laamann, and R. D. Hudson, 1991: Evaluation of the NOAA-11 solar backscatter ultraviolet radiometer, Mod 2 (SBUV/2): Inflight calibration. *Calibration of Passive Remote Observing Optical and Microwave Instrumentation*, B. W. Guenther, Ed., International Society for Optical Engineering (SPIE Proceedings, Vol. 1493), 80–90, doi:10.1117/12.46686.

Wielicki, B. A., and Coauthors, 1998: Clouds and the Earth's Radiant Energy System (CERES): Algorithm overview. *IEEE Trans. Geosci. Remote Sens.*, **36**, 1127–1141, doi:10.1109/36.701020.

——, B. R. Barkstrom, E. F. Harrison, R. B. Lee III, G. L. Smith, and J. E. Cooper, 1996: Clouds and the Earth's Radiant Energy System (CERES): An Earth Observing System Experiment. *Bull. Amer. Meteor. Soc.*, **77**, 853–868, doi:10.1175/1520-0477(1996)077<0853:CATERE>2.0.CO;2.

Zhang, Y.-C., W. B. Rossow, A. A. Lacis, V. Oinas, and M. I. Mishchenko, 2004: Calculation of radiative fluxes from the surface to top of atmosphere based on ISCCP and other global data sets: Refinements of the radiative transfer model and the input data. *J. Geophys. Res.*, **109**, D19105, doi:10.1029/2003JD004457.